Pergamon

PII: S0045-7949(96)00158-7

Computers & Structures Vol. 64, No. 1–4, pp. 603–621, 1997

Printed in Great Britain
0045-7949/97 $17.00 + 0.00

HOMOGENIZATION-BASED ANALYSIS AND DESIGN OF COMPOSITES

C. C. Swan and **I. Kosaka**

Department of Civil and Environmental Engineering, The University of Iowa, Iowa City, IA 52242, U.S.A.

Abstract—Computational homogenization is demonstrated as a potent analysis tool that can be used directly to predict the property–structure relationships of many existing classes of composites, and indirectly to design the topological macrostructure of new generations of composites so as to optimize their mechanical properties. This paper lays out the homogenization analysis problem for general classes of inelastic mechanical composites. The analysis techniques presented are logically divided into stress- and strain-controlled methods, both of which are formulated for periodic composites in a finite element setting. A well-recognized issue with computational homogenization is that for three-dimensional structures associated computing costs escalate rapidly with mesh refinement, thus providing a potential obstacle to usage of the method. To address this important issue, the relative performance of alternative vector and parallel numerical algorithms that facilitate high speed and efficiency with computing resources are compared on sample homogenization computations of inelastic Byzantine masonry and modern graphite–epoxy. Building upon the established homogenization analysis framework, a novel method for designing the topology of a composite's macrostructure is then formulated, implemented and demonstrated to achieve new material designs with significantly enhanced mechanical performance properties. © 1997 Civil-Comp Ltd and Elsevier Science Ltd.

1. INTRODUCTION

1.1. *Optimal design of structures and materials*

A review of the literature [1–9] shows that computer-based design methods for structural optimization are enjoying rapid development, in contrast to methods for the computer-based optimal design of composite materials. Nevertheless, using the concept of material and structural hierarchy [10], a strong analogy exists between the design of large scale civil/mechanical structural systems and the macrostructural design and layout of composite materials. (The term "macrostructure" in this paper will denote the shape, size and arrangement of the "homogeneous" material phases throughout a composite medium, with associated length scales typically ranging from microns to centimeters.) While composite materials systems are obviously designed at much smaller length scales than civil/mechanical structures, their design is similar in that they too require optimization of both mechanical and thermal load transfer systems subject to numerous constraints. Since the analogy between structural and material design optimization will be exploited here, it is proposed that the recent history of computer-based structural design optimization can be classified into three stages of development:

stage 1—general, automated methods are developed for analysis of a broad class of structures;

stage 2—analysis tools are employed inside of optimization programs to design structures in an automated and optimized fashion;

stage 3—analysis, optimization, and design sensitivity analysis tools are rapidly refined so that ever broader classes of structures and structural behaviors (including failure behaviors) can be efficiently handled in the procedure.

Noting the spectrum of advanced applications being undertaken, it can be argued that structural optimization research is currently entering the third stage of development where it is providing a driving impetus for harnessing high-performance computing methods in applied mechanics to drive the cost of computerized analysis and design ever downwards [11, 12]. In contrast, it appears that computer-based design optimization of composite materials is presently in the second stage of development with relatively few efforts reported [13–15] at integrated topological design optimization of composite macrostructures. One intent of this paper is to demonstrate that by harnessing homogenization-based micro/macro mechanics techniques with accepted structural optimization methods, the design of composite macrostructures is poised to make rapid, substantial gains.

Computer-based geometric design and layout of composite macrostructures can for simplicity be subdivided into: (a) parametric design optimization

methods; and (b) more general nonparametric methods. In parametric design methods, the designer from the outset decides what class of geometric design will be achieved, and specifies a few well-chosen parameters that characterize designs from the chosen class. For example, in the tailoring of laminated composites, one decides *a priori* upon a fibrous laminated material macrostructure and in the design process, the parameters (fiber spacing, lamina thicknesses, ply orientations and stacking sequences) are systematically chosen to optimize desired mechanical and thermal material performance. Tailoring has been developed extensively and applied to a wide variety of fiber-reinforced laminated composites by numerous investigators. Among the many design issues that have been successfully addressed in tailoring are damping [16], reduction of residual thermal stresses by interphase design in metal matrix composites [17] and enhancement of fatigue strengths [18]. A limitation of parametric design methods and tailoring in particular, however, is that one always arrives in the end at the predetermined class of composite (laminated) with its inherent weaknesses (tendency toward delamination due to lack of reinforcement between layers). It is further recognized that the layup process suitable for laminated composites is infeasible for many thick-sectioned or irregular structural members.

In more general nonparametric methods, the designer does not impose the class of the final design configuration at the onset, but rather allows the design method itself to solve for the configuration (or topology) that will ultimately yield the best overall performance of the system [3, 19]. Since this type of method draws from a broader class of design solutions compared to parametric methods, it is ultimately capable of arriving at designs that yield significantly higher performance. An example of such nonparametric design methods is topological structural optimization which purchases its generality by employing many more design variables than do parametric methods.

1.2. *Property–structure analysis of composites*

When performing analysis and design of structures built of composites, it is efficient to treat the heterogeneous composite medium as a homogeneous "effective medium" characterized by the "effective" mechanical properties of the composite [20, 21]. Rigorous asymptotic analysis [22] shows this approximation to be valid when

$$\frac{l_i}{\lambda_i} \gg 1, \quad i = 1, 2, 3, \tag{1}$$

where the l_i represents the smaller of the body's dimensions or the length scale of variation in loads applied to the body, and the λ_i denotes the characteristic dimensions of a representative volume element of the composite or the unit cell. Assuming that the effective medium approximation can be safely invoked, vital issues of longstanding interest to applied mechanicians that must then be addressed in solving analysis problems are: (1) determining appropriate forms of effective medium constitutive models for composites; and (2) parameter estimation in such constitutive models for specific composites.

A related question to be taken up here is how to design the composite to optimize targeted effective mechanical properties. The bounds literature provides quantitative upper and lower limits on the strengths [23–25], stiffnesses [26–28] and conductivities [26–28] that can be achieved when combining discrete solids. Nevertheless, with the exception of a few specialized composite design techniques [29, 30], general design methods that tell how to spatially arrange the solids in the composite's macrostructure to achieve the optimal properties remain to be developed. This effort begins to address this issue.

At present, both analytical and computational micro-/macro-mechanical methods are being actively applied as complementary frameworks for characterizing effective mechanical behaviors of composite material systems. There exists a well-recognized tradeoff between the frameworks—due to their elegance and efficiency, analytical methods (if they can be realistically applied) are preferred. Specific analytical methods have been developed for composites that are particulate reinforced [31], aligned fiber reinforced [32, 33], mesh and weave reinforced [34, 35] and short chopped-fiber reinforced [36], as examples. Since each method generally imposes both geometric and constitutive assumptions, each is of limited generality. When these methods prove to be insufficient, researchers then turn to more robust computational methods such as Aboudi's generalized method of cells [37] or computational homogenization. These methods are being increasingly used for complex material systems, with a wide breadth of published applications and a capability to handle arbitrarily complex macrostructures with highly nonlinear internal phenomenology such as general inelasticity [38, 39], nonlocal constitutive behaviors, softening, strain localization and micro-cracking [40], finite deformation [41] and phase debonding [37].

A detailed comparison of the tradeoffs between these approaches is beyond the scope of this work. Instead, the intent of this paper is to present computational homogenization as a potent and general method for addressing both the analysis and design issues mentioned above. While the method can be applied to materials having arbitrary macrostructures, it is most efficient with periodic composites. Among the materials in this category are many fibrous (woven, meshed, stitched, or aligned), cellular (honeycombed) and masonry composites. Using the host of developments in nonlinear computational solid mechanics over the past two decades, computational homogenization now has the capability to

address for both analysis and design purposes most of the nonlinear phenomena occurring within composites. The remaining issue is cost.

Stated bluntly, computational homogenization of three-dimensional inelastic composites is a challenging proposition that can require considerable computing resources. The unit cell on which computations are performed is generally three-dimensional and the structure therein must be meshed at moderate to high refinement to obtain accurate results. Nonlinear inelastic material behaviors require extensive effort at both the global level where finite element force balance equations must be solved iteratively, and at the local element and stress point levels, where the nonlinear constitutive equations must be solved repeatedly. Given the intensiveness of the task, efficient algorithms must be employed to minimize solution times and associated costs. While many configurations are possible, it is here assumed that the computations will be performed on shared memory multi-CPU vector processing machines (e.g. Cray, Convex, SGI, IBM, etc.).

1.3. *Scope of paper*

The sequence of this paper is as follows. In Section 2, the cell problem for homogenization of inelastic periodic composites is formulated in a finite element setting. To address the cost of homogenization computations, attention is devoted in Section 3 to the following algorithms for solving the associated nonlinear algebraic finite element equations: Newton's method with high-performance vector and parallel equation solvers; Newton's method with a jacobi preconditioned conjugate gradient (JCG) solver; and a memoriless BFGS algorithm. Vector-parallel element level operations germane to all three solution methods are discussed. The relative performance of the methods is demonstrated in Section 4 on both elasto-plastic masonry and a graphite–epoxy fibrous composite. Having established a general and robust framework for analysis, the issue of designing enhanced composites using a novel homogenization based optimization framework is then presented and demonstrated in Section 5.

2. HOMOGENIZATION OF PERIODIC MEDIA

2.1. *Notation for periodic media*

The heterogeneous body under consideration, which could be a structure or a structural member, for example, occupies a domain Ω_b in $\mathscr{R}^3$ (Fig. 1) and exhibits a periodic structure in that it consists of repeating, identical subdomains each of which is a unit cell $\Omega_s = \Pi_{i=1}^3]0, \lambda_i[$, where λ_i are the dimensions of the cell and hence the "wavelengths" of the macrostructure [42]. A material point in the undeformed cell Ω_s is referenced by its local microscale material coordinates X_i, while the same point in the larger domain Ω_b is referenced by its macroscale coordinates Y_i. The microscale coordinates are employed in solving the cell problem, while the macroscale coordinates are used in solving global boundary value problems (such as structural analysis problems) with the effective medium approximation.

Our objective is to isolate a unit cell Ω_s from the larger body Ω_b and to numerically perform experiments on it to obtain the effective mechanical properties of the medium. The complexity lies in getting the isolated unit cell Ω_s to respond as if it were still embedded in Ω_b during the experiments. A fundamental concept of great utility in this regard is to require that the stress σ and strain ϵ fields in all cells be identical under macroscopically uniform loading as has been proposed in Refs [42–44]. These fields are identical in all cells when they are λ-periodic such that

$$\epsilon(Y_1, Y_2, Y_3) = \epsilon(Y_1 + n_1\lambda_1, Y_2 + n_2\lambda_2, Y_3 + n_3\lambda_3), \tag{2a}$$

$$\sigma(Y_1, Y_2, Y_3) = \sigma(Y_1 + n_1\lambda_1, Y_2 + n_2\lambda_2, Y_3 + n_3\lambda_3), \tag{2b}$$

where n_1, n_2, n_3 are arbitrary integers. Periodicity of one field typically assures periodicity of the other and suggests that they admit additive decompositions into uniform macroscopic contributions (**S**, **E**) and oscillatory contributions (σ^*, ϵ^*) that vary over the unit cell:

$$\sigma(\mathbf{Y}) = \mathbf{S} + \sigma^*(\mathbf{Y}), \quad \epsilon(\mathbf{Y}) = \mathbf{E} + \epsilon^*(\mathbf{Y}). \tag{3}$$

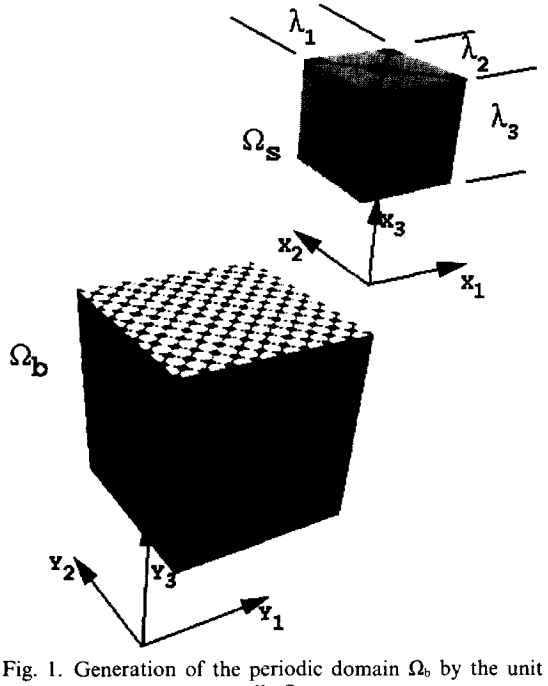

Fig. 1. Generation of the periodic domain Ω_b by the unit cells Ω_s.

The macroscopic quantities are defined as volume averages over the unit cell such that

$$\mathbf{S} = \langle \sigma \rangle = \frac{1}{V} \int_{\Omega_s} \sigma \, d\Omega, \quad \mathbf{E} = \langle \epsilon \rangle = \frac{1}{V} \int_{\Omega_s} \epsilon \, d\Omega. \quad (4)$$

Combining eqns (3) and (4) it is readily apparent that

$$\langle \sigma^* \rangle = 0, \quad \langle \epsilon^* \rangle = 0. \quad (5)$$

Remark. Strictly speaking, eqn $(4)_2$ is valid only when the unit cell Ω_s contains no macroscopic holes or voids. By assuming that the holes are filled with a highly compliant material, however, eqn $(4)_2$ can still be used.

With regard to the constant-periodic decomposition of the strain field, it can be shown by integrating eqn $(3)_2$ that the displacement field must admit a linear-periodic decomposition. The respective displacement fields on Ω_b and Ω_s are thus

$$\mathbf{u}(\mathbf{Y}) = \mathbf{E}\mathbf{Y} + \mathbf{u}^*_{\text{per}}(\mathbf{Y}), \quad (6a)$$

$$\mathbf{u}(\mathbf{X}) = \mathbf{E}\mathbf{X} + \mathbf{u}^*_{\text{per}}(\mathbf{X}), \quad (6b)$$

where rigid body contributions are eliminated by proper restraints on the domain (Ω_b or Ω_s).

As with laboratory experiments, there are two distinct procedures for performing numerical experiments on unit cells: the stress- and strain-controlled methods. The generic stress-controlled homogenization problem involves imposing a history of $\mathbf{S}(\tau)$ on the unit cell and computing the corresponding history of $\mathbf{E}(\tau)$ while the strain-controlled homogenization problem involves imposing a history of macroscopic strain $\mathbf{E}(\tau)$ and computing the corresponding history of macroscopic stress $\mathbf{S}(\tau)$. In the preceding, τ plays the role of a time-like loading parameter.

The objective is to perform these computations using general purpose finite element computer codes. Within the framework of displacement finite element methods, the implementational details of the two methods are quite different. However, since it is advantageous to have both methods at one's disposal when analyzing and designing composites, both are formulated below.

2.2. *Stress-controlled method*

2.2.1. *Surface compatibility*. Typically a parallelepiped, the bounding surface of a unit cell Ω_s is composed of three surface pairs $\Gamma_s = \Gamma_1 \cup \Gamma_2 \cup \Gamma_3$ where the pth pair ($p = 1, 2, 3$) is composed of opposing faces, and thus satisfies $\Gamma_{p_1} \cup \Gamma_{p_2} = \Gamma_p$ and $\Gamma_{p_1} \cap \Gamma_{p_2} = \{\emptyset\}$. Due to the periodicity of the domain Ω_b, the surfaces comprising each pair must be geometrically identical to each other in the sense of size, shape, orientation and the macrostructure showing on each surface. Such surface pairs are said to be compatible.

A criterion for the maintenance of surface compatibility is briefly proposed, and to simplify presentation, attention is focused on the pth pair of a given unit cell. So that a one-to-one correspondence can be drawn between material points on the surface pairs, identical two-dimensional Lagrangian parameterizations are assigned to each surface Γ_{p_1} and Γ_{p_2} of the pair in the undeformed state such that

$$\mathbf{X}_1(\xi, \eta) \in \Gamma_{p_1}, \quad \mathbf{X}_2(\xi, \eta) \in \Gamma_{p_2} \quad \xi, \eta \in [-1, 1]. \quad (7)$$

A sufficient condition for the surfaces Γ_{p_1} and Γ_{p_2} to be of identical shape, size, and spatial distribution in all deformed states is that they remain identically distributed with respect to the parameterizations about their geometric centroids. Assuming that this holds true in the undeformed state, it will also hold true in the deformed state [38] if the following displacement criterion is satisfied:

$$(\mathbf{u}^p_1(\xi, \eta) - \tilde{\mathbf{u}}^p_1) = (\mathbf{u}^p_2(\xi, \eta) - \tilde{\mathbf{u}}^p_2), \quad (8)$$

in which

$$\tilde{\mathbf{u}}^p_i = \frac{\int_{\square} \mathbf{u}^p_i(\xi, \eta) J_i \, d\square}{\int_{\square} J_i \, d\square}, \quad i = 1, 2, \quad (9a)$$

$$J_i = \det\left[\frac{\partial \mathbf{X}_i}{\partial \xi}\right], \quad i = 1, 2. \quad (9b)$$

As an example, and to make this point very clear, a two-dimensional unit cell of masonry which undergoes a uniaxial stress test along the vertical axis is shown below in Fig. 2. Figure 2b shows a state of incompatible deformation in that eqn (8) is not satisfied on the boundaries; in contrast, Fig. 2c shows a state of compatible deformation in that eqn (8) is uniformly satisfied on the boundaries.

For numerical implementations, it is useful to define the residuals of this criterion, eqn (8), as incompatible displacement fields $\mathbf{b}^{p^1}$ and $\mathbf{b}^{p^2}$ over the respective surfaces Γ_{p_1} and Γ_{p_2} as

$$\mathbf{b}^{p^1}(\xi, \eta) := (\mathbf{u}^p_1(\xi, \eta) - \tilde{\mathbf{u}}^p_1) - (\mathbf{u}^p_2(\xi, \eta) - \tilde{\mathbf{u}}^p_2), \quad (10a)$$

$$\mathbf{b}^{p^2}(\xi, \eta) := (\mathbf{u}^p_2(\xi, \eta) - \tilde{\mathbf{u}}^p_2) - (\mathbf{u}^p_1(\xi, \eta) - \tilde{\mathbf{u}}^p_1). \quad (10b)$$

The criterion for surface compatibility is thus satisfied for a given surface pair if the incompatible displacement fields vanish at each point in the parameter domain $\xi, \eta \in [-1, 1]$.

2.2.2. *Finite element implementation*. The strong form of the stress-controlled homogenization problem, taking account of surface compatibility

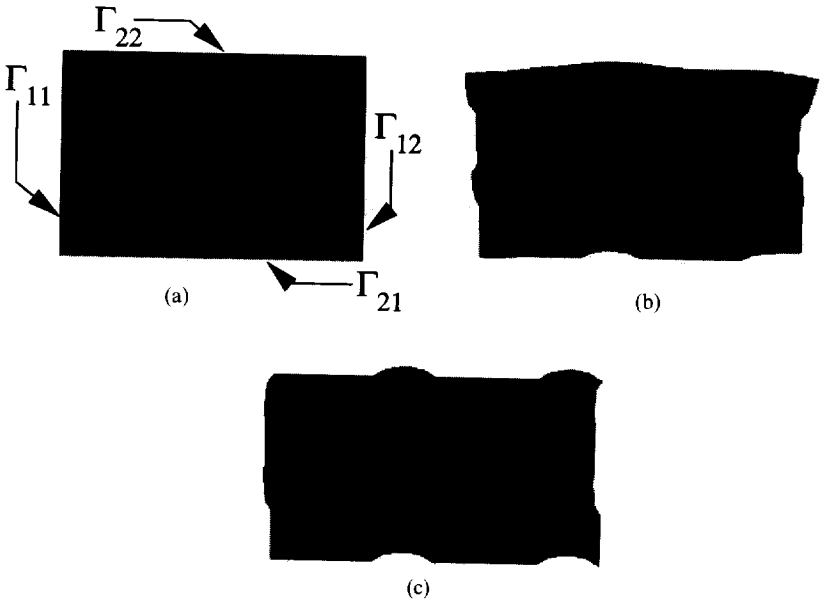

Fig. 2. (a) Undeformed unit cell; (b) incompatibly deformed unit cell; and (c) compatibly deformed unit cell of thickly jointed and staggered masonry undergoing a uniaxial stress test.

constraints, is written as follows. Find $\mathbf{u}: \bar{\Omega}_s \mapsto \mathscr{R}^3$ such that:

$$\sigma_{ij,i} = 0 \quad \text{in } \Omega_s, \tag{11}$$

$$b_j^{p^1} = 0 \quad \text{on } \Gamma_{p_1} \text{ for } p = 1, 2, 3, \tag{12}$$

$$b_j^{p^2} = 0 \quad \text{on } \Gamma_{p_2} \text{ for } p = 1, 2, 3. \tag{13}$$

Subject to the boundary conditions:

$$u_j = g_j \quad \text{on } \Gamma_{g_j} \quad \text{for } j = 1, 2, 3, \tag{14}$$

$$n_i\sigma_{ij} = h_j \quad \text{on } \Gamma_{h_j} \quad \text{for } j = 1, 2, 3, \tag{15}$$

where Γ_g and Γ_h are, respectively, the mutually exclusive portions of the boundary on which essential and natural (traction) conditions are applied. The applied surface tractions h_j have the decomposition

$$h_j = \bar{h}_j + h_j^*, \tag{16}$$

in which

$$\bar{h}_j = n_j S_{ij}, \tag{17a}$$

$$h_j^* = n_j\sigma_{ij}^*. \tag{17b}$$

While $\bar{h}_j$ is known and prescribed on the boundaries, h_j^* is initially unknown and is obtained from the compatibility constraints. Furthermore, essential boundary conditions, eqn (14), are prescribed only to restrain the rigid body modes of the unit cell. Constitutive models relating stress and strain are introduced in Sections 4 and 5.

The finite element formulation of this problem is largely standard, the only unique aspect being that of the surface compatibility constraints, eqns (12) and (13). In the computations presented in Section 4, the surface compatibility constraints are enforced by using "compatible surface elements" which rely on a penalty function implementation. Implementational details of the compatible surface elements have been prescribed at length in Ref. [38] and will not be discussed here. As implemented, these elements are completely modular.

2.3. *Strain-controlled method*

In strain-controlled homogenization computations, a linear displacement field (**EX**) arising from an applied macroscopic strain **E** is imposed on the unit cell Ω_s, and a variational problem is solved for the periodic part $\mathbf{u}^*_{\text{per}}$. In the absence of body forces the variational form of equilibrium is written as

$$\int_{\Omega_s} \sigma_{ij,i}\delta u_j \, d\Omega = 0. \tag{18}$$

Recalling eqn (6b), the total displacement field on Ω_s possesses the decomposition

$$\mathbf{u} = \mathbf{EX} + \mathbf{u}^*_{\text{per}}, \tag{19}$$

in which the first term on the right side is fully prescribed, and the periodic part is that which remains to be determined. Hence the variation

of eqn (19) $\delta\mathbf{u}$ is purely periodic, and the variational form, eqn (18), reduces to

$$\int_{\Omega_s} \sigma : \epsilon^*(\delta\mathbf{u})\, d\Omega = \int_{\Gamma} \sigma^n \cdot \delta\mathbf{u}\, d\Gamma. \tag{20}$$

If the right side of this expression is interpreted as the contribution of tractions on the exterior of the unit cell, then it must vanish due to the periodicity of σ and $\delta\mathbf{u}$. Thus the final weak form to be implemented is written

$$\int_{\Omega_s} \sigma(\mathbf{u}) : \epsilon^*(\delta\mathbf{u})\, d\Omega = 0. \tag{21}$$

Applying a Galerkin finite element implementation, the mesh approximations to $\delta\mathbf{u}$ and $\mathbf{u}$ are

$$u_i \to u_i^h = \mathbf{EX} + \sum_{B=1}^{n-n_{g_i}} d_{B_i} N_B(\mathbf{X}) + \sum_{E=1}^{n_{g_i}} g_{E_i} N_E(\mathbf{X}), \tag{22a}$$

$$\delta u_i \to \delta u_i^h = \sum_{A=1}^{n-n_{g_i}} c_{A_i} N_A(\mathbf{X}). \tag{22b}$$

Above, the N_A, N_B, N_E are standard nodal shape functions satisfying the usual requirements of linear independence and continuity while n denotes the number of nodes in the mesh and n_{g_i} the nodes at which u_i is prescribed. As for the stress-controlled problem, essential boundary conditions are prescribed only to restrain the rigid body modes of the unit cell. Implementing these forms in eqn (21) and simplifying gives the FEM nodal force balance equations:

$$\mathbf{r}_A = \int_{\Omega_s} \mathbf{B}_A^{\mathrm{T}} \sigma(\mathbf{u}^h)\, d\Omega = 0, \quad A \in \{n - n_g\}, \tag{23}$$

in which $\mathbf{B}_A$ are nodal strain displacement matrices and $\sigma(\mathbf{u}^h)$ is the stress field as a function of the total displacement field.

In keeping with standard solution techniques for nonlinear finite element equations, eqn (23) is solved incrementally. Specifically, a linear-periodic displacement predictor–corrector technique is applied in which the predictor is the linear part of the displacement field $\mathbf{E}(\tau_{n+1})\mathbf{X}$, and subsequent correctors to the displacement field are periodic. At the $(n+1)$th time or load step, one has from the previous step the equilibrium nodal displacement field $\mathbf{d}^n$ as well as the stress and internal state variable fields. The displacement predictor $\tilde{\mathbf{d}}$ at the Ath nodal point in the mesh discretization for the $(n+1)$th step is simply

$$\tilde{\mathbf{d}}_A^{n+1} = \mathbf{d}_A^n + [\mathbf{E}(\tau_{n+1}) - \mathbf{E}(\tau_n)]\mathbf{X}_A. \tag{24}$$

In keeping with the displacement predictor, the initial nodal residual forces are

$$\tilde{\mathbf{r}}_A = \int_{\Omega_s} \mathbf{B}_A^{\mathrm{T}} \sigma(\tilde{\mathbf{u}}^h)\, d\Omega. \tag{25}$$

In all subsequent iterations to obtain nodal force balance for the given load step, corrections to the displacement field are periodic. Hence the displacement field satisfies the linear-periodic decomposition since it is composed of a sequence of linear prediction updates and a sequence of periodic corrector updates.

In practice, periodicity of the correction displacement fields is effectively achieved by a nodal enslavement procedure in which corresponding nodes on opposite faces of the unit cell Ω_s share the same equation numbers. Thus, in a finite element setting, the only nonstandard operations required in strain-controlled homogenization computations are those associated with the linear displacement field predictor.

Remark. In the meshing of the unit cell Ω_s, it is assumed that a one-to-one correspondence exists between nodes on opposing faces of the unit cell.

3. SOLUTION METHODS

In the past two decades much work has been done on solution algorithms for large scale finite element systems, to take advantage of vector and parallel computing capabilities. Among the many considered have been domain decomposition methods [45, 46], parallel direct equation solvers [11, 12, 47], and preconditioning techniques for scalable iterative equation solvers. In this section, the usage of high performance vector and parallel equation solvers and scalable iterative equation solving algorithms on homogenization of inelastic composites is investigated.

Due to their reduced memory requirements and ease of parallelization on most computing architectures, iterative equation solving methods such as preconditioned conjugate gradient (PCG) methods and memoriless quasi-Newton methods that have good performance characteristics have been highly sought after. The remaining difficulty with such methods today lies in finding reliable preconditioning methods that do not compromise the inherent benefits of iterative equation solvers. Their reduced memory requirements and ease of parallelization makes the usage of iterative solution methods potentially very attractive in homogenization computations.

High-performance equation solvers have also been under intense development and now show impressive performance, especially on vector and parallel machines. The equation solvers are particularly effective on shared memory multi-processing systems

that have large RAM (random access memory) or SSD (solid state disk) capacities.

In this section, we present three algorithms for solving nonlinear finite element homogenization equations: Newton's method with high performance equation solvers; Newton's method with a JCG solver; and a memoriless BFGS equation solving algorithm. Each of the three algorithms which are applied in Section 4 require varying allotments of computational effort at both the global level and at the element level. To achieve optimal performance across all methods, both global algorithms and local element algorithms must be optimized. Optimization of element operations is emphasized in this section.

3.1. *Newton's method*

It is recalled that the system of nonlinear global force–balance equations to be solved for both stress- and strain-controlled homogenization computations has the form

$$\mathbf{r}(\mathbf{d}) = 0, \tag{26}$$

where $\mathbf{d}$ is the field of nodal displacements. For a fixed load or time step, the employment of Newton's method in tandem with a line search yields a recursive sequence of the global displacement vectors $\mathbf{d}_{n+1}$ that eventually solves eqn (26). The sequence to update the global displacement vector at the $(n+1)$th load or time step is shown in Box 1.

In Box 1, $\mathbf{K}$ is the global tangent stiffness matrix and α_k is the search parameter chosen to satisfy the standard line search criterion $|\delta_k^{\mathrm{T}}\mathbf{r}^{k+1}| < \mathrm{STOL}$ [48], in which STOL is a tolerance parameter controlling the accuracy of the search. In the linear solving phase, eqn (27), $\mathbf{K}$ can be updated each iteration (pure Newton) or updated only periodically (modified Newton). Within the context of a global Newton algorithm, numerous options are available to complete the linear solving operation (27). The options considered are direct solution (noniterative) with high performance equation solvers and iterative JCG solution.

Predictor phase

$k = 0$: counter initialization

$\mathbf{d}_{n+1}^{k} = \tilde{\mathbf{d}}_{n+1}$: displacement predictor

form $\mathbf{r}_{n+1}^{k}(\mathbf{d}_{n+1}^{k})$: initial residual.

Corrector phase

while $(\|\mathbf{r}_{n+1}^{k}\| > \mathrm{RTOL})$,

$\mathbf{K}\delta_k = -\mathbf{r}_{n-1}^{k}$: linear solving phase (27)

$\mathbf{p}_k = \alpha_k \delta_k$: line search (28)

$\mathbf{d}_{n+1}^{k+1} = \mathbf{d}_{n+1}^{k} + \mathbf{p}_k$: displacement update (29)

form $\mathbf{r}_{n+1}^{k+1}(\mathbf{d}_{n+1}^{k+1})$: residual update

$k = k + 1$: counter update

end-while.

Box 1. Global Newton solving algorithm.

3.1.1. *Direct equation solvers.* With direct equation solving methods, the global tangent stiffness matrix is formed and stored in either a skyline, profile or sparse format. Despite the efficiency of these formats, the memory required for large three-dimensional problems can still be problematic. Nevertheless, the speed of direct high-performance solvers makes their usage in finite element applications very promising [47]. The parallel and vector equation solvers of Storaasli *et al.* using skyline [11] and profile [12] Cholesky factorization have been implemented and used in this effort. They have been demonstrated to have attainable performances well into the GFLOP range (billions of floating point operations per wall clock second) when run on multi-processor Cray machines. Because it uses "saxpy" operations ($\mathbf{s} = \alpha\mathbf{x} + \mathbf{y}$), the profile algorithm is roughly twice as fast on Cray machines as the skyline algorithm which employs vector unrolling of dot products. On the other hand, the memory required by the profile solver is generally greater (0–200%) than that required by the skyline solver.

3.1.2. *JCG solver.* An alternative to using high performance equation direct equation solvers in step (27) of the global Newton algorithm is to use a conjugate gradient method. Here, the JCG algorithm presented by Hughes *et al.* [49] is employed because of its relative simplicity and good performance characteristics. (A competing EBE preconditioner of marginally superior performance was also presented in Ref. [49].) The JCG method treats eqn (27) as the generic linear algebra problem $\mathbf{Ax} = \mathbf{b}$ in which $\mathbf{A}$ is assumed to be symmetric and positive definite. The JCG algorithm for solving this generic problem is shown in Box 2.

Step 1: *initialize*

$m = 0, \quad \mathbf{x}_m = 0, \quad \mathbf{s}_m = \mathbf{b},$

$\mathbf{g}_m = \mathbf{z}_m = \mathbf{B}^{-1}\mathbf{s}_m.$

Step 2: *line search and updates*

$$\alpha_m = \frac{\mathbf{s}_m \cdot \mathbf{z}_m}{\mathbf{g}_m \cdot \mathbf{A}\mathbf{g}_m}, \tag{30}$$

$$\mathbf{x}_{m+1} = \mathbf{x}_m + \alpha_m \mathbf{g}_m, \tag{31}$$

$$\mathbf{s}_{m+1} = \mathbf{s}_m - \alpha_m \mathbf{A}\mathbf{g}_m. \tag{32}$$

Step 3: *if* $\|\mathbf{s}_{m+1}\| \leqslant \delta_{\mathrm{L}} \|\mathbf{s}_0\|$, *return*

Step 4: *update conjugate search direction*

$$\mathbf{z}_{m+1} = \mathbf{B}^{-1}\mathbf{s}_{m+1}, \tag{33}$$

$$\beta_m = \frac{\mathbf{s}_{m+1} \cdot \mathbf{z}_{m+1}}{\mathbf{s}_m \cdot \mathbf{z}_m}, \tag{34}$$

$$\mathbf{g}_{m+1} = \mathbf{z}_{m+1} + \beta_m \mathbf{g}_m, \tag{35}$$

$$m = m + 1.$$

Go to Step 2.

Box 2. JCG algorithm to solve $\mathbf{Ax} = \mathbf{b}$.

The advantage of this JCG algorithm is that the global stiffness matrix **K** (or **A**) need not be formed or factorized. Operations in Box 2 involving the product **Ag** [eqns (30) and (32)] are performed not at global level, but rather at the element level by storing and utilizing element contributions to **A**. The memory required to store all element contributions to **A** is usually substantially less than storing the assembled **A**.

The preconditioner **B** is here chosen as diag[**K**(**d**)]. The rate of convergence in the energy norm $\|\mathbf{x}_m\|_{\mathbf{A}} \equiv (\mathbf{x}_m \cdot \mathbf{A}\mathbf{x}_m)^{1/2}$ is bounded [49, 50]:

$$\|\mathbf{x}_{m+1} - \mathbf{x}_m\|_{\mathbf{A}} \leqslant \left(\frac{\sqrt{C}-1}{\sqrt{C}+1}\right)\|\mathbf{x}_m - \mathbf{x}\|_{\mathbf{A}},$$

where C is the condition number:

$$C(\mathbf{B}^{-1}\mathbf{A}) = \max_i(\tilde{\lambda}_i)/\min_i(\tilde{\lambda}_i),$$

in which the $\tilde{\lambda}_i$ are the eigenvalues of $\mathbf{B}^{-1}\mathbf{A}$ [51]. To hasten the rate of convergence, the following behavior in the preconditioner is sought: $C(\mathbf{B}^{-1}\mathbf{A}) \rightarrow 1$.

3.2. *Memoriless quasi-Newton algorithm*

A potentially viable alternative to the Newton algorithm is Shanno's memoriless BFGS algorithm [52], which follows directly from the common BFGS solution method [53, 54]. Rather than using the Newton sequence of Box 1 to solve the global force balance eqn (26), the quasi-Newton sequence is used:

$$\delta_k = -\hat{\mathbf{H}}_{k+1}\mathbf{y}_k, \tag{36}$$

$$\mathbf{p}_k = \alpha_k \delta_k, \tag{37}$$

$$\mathbf{d}_{k+1} = \mathbf{d}_k + \mathbf{p}_k. \tag{38}$$

Equation (36) is the so-called quasi-Newton equation in which

$$\mathbf{y}_k := \mathbf{r}_{k+1} - \mathbf{r}_k, \tag{39}$$

and in which $\hat{\mathbf{H}}$ denotes an approximation to the true inverse Jacobian matrix $\mathbf{H} = \mathbf{K}^{-1}$. The recursive BFGS formula for a rank-two update of the inverse Jacobian matrix is [54]:

$$\hat{\mathbf{H}}_{k+1} = \hat{\mathbf{H}}_k + \left(1 + \frac{\mathbf{y}_k^{\mathrm{T}}\hat{\mathbf{H}}_k\mathbf{y}_k}{\mathbf{p}_k^{\mathrm{T}}\mathbf{y}_k}\right)\left(\frac{\mathbf{p}_k\mathbf{p}_k^{\mathrm{T}}}{\mathbf{p}_k^{\mathrm{T}}\mathbf{y}_k}\right) - \frac{\mathbf{p}_k\mathbf{y}_k^{\mathrm{T}}\hat{\mathbf{H}}_k + \hat{\mathbf{H}}_k\mathbf{y}_k\mathbf{p}_k^{\mathrm{T}}}{\mathbf{p}_k^{\mathrm{T}}\mathbf{y}_k}. \tag{40}$$

If the BFGS update of $\hat{\mathbf{H}}$ retains no memory of the previous iterate, then the approximation $\hat{\mathbf{H}}_{k+1}$ is obtained from an unchanging matrix **Z** rather than the previous iterate $\hat{\mathbf{H}}_k$. Replacing $\hat{\mathbf{H}}_k$ by **Z** in eqn (40) yields Shanno's memoriless BFGS update formula:

$$\hat{\mathbf{H}}_{k+1} = \mathbf{Z} + \left(1 + \frac{\mathbf{y}_k^{\mathrm{T}}\mathbf{Z}\mathbf{y}_k}{\mathbf{p}_k^{\mathrm{T}}\mathbf{y}_k}\right)\left(\frac{\mathbf{p}_k\mathbf{p}_k^{\mathrm{T}}}{\mathbf{p}_k^{\mathrm{T}}\mathbf{y}_k}\right) - \frac{\mathbf{p}_k\mathbf{y}_k^{\mathrm{T}}\mathbf{Z} + \mathbf{Z}\mathbf{y}_k\mathbf{p}_k^{\mathrm{T}}}{\mathbf{p}_k^{\mathrm{T}}\mathbf{y}_k}, \tag{41}$$

where **Z** is preferably a diagonal matrix to minimize the storage and computation required of the algorithm. While Shanno [52] suggested $\mathbf{Z} = \mathbf{I}$, we here employ the inverted diagonal entries of the global Jacobian matrix (e.g. $\mathbf{Z} = \mathbf{B}^{-1} = [\mathrm{diag}\,\mathbf{K}]^{-1}$). Utilizing eqn (41) in the search direction update eqn (36) yields

$$\delta_k = -\mathbf{Z}\mathbf{r}_{k+1} + \left(\frac{\mathbf{p}_k^{\mathrm{T}}\mathbf{r}_{k+1}}{\mathbf{p}_k^{\mathrm{T}}\mathbf{y}_k}\right)\mathbf{Z}\mathbf{y}_k - \left[\left(1 + \frac{\mathbf{y}_k^{\mathrm{T}}\mathbf{Z}\mathbf{y}_k}{\mathbf{p}_k^{\mathrm{T}}\mathbf{y}_k}\right)\left(\frac{\mathbf{p}_k^{\mathrm{T}}\mathbf{r}_{k+1}}{\mathbf{p}_k^{\mathrm{T}}\mathbf{y}_k}\right) - \frac{\mathbf{y}_k^{\mathrm{T}}\mathbf{Z}\mathbf{r}_{k+1}}{\mathbf{p}_k^{\mathrm{T}}\mathbf{y}_k}\right]\mathbf{p}_k. \tag{42}$$

Remark. If an exact line search is performed, then terms containing $\mathbf{p}_k^{\mathrm{T}}\mathbf{r}_{k+1}$ in eqn (42) vanish. In this case, the update is identical to that produced in the JCG algorithm. Thus this method is essentially a JCG algorithm taking account of inaccuracies in the line search. Unlike the JCG algorithm, however, this algorithm does not assume an underlying quadratic objective function. Hence the line search and force updates are nontrivial and require substantially more effort. The advantage, however, is that the element contributions to **K** are not required and consequently this method requires substantially less memory than even the JCG algorithm presented which does store the element contributions to **K**. The reduced memory requirements are demonstrated in Section 4. As with the JCG algorithm, the rate of convergence with this algorithm is governed by the effectiveness of the preconditioning matrix **B**.

3.3. *Vector–parallel element operations*

Depending on the global algorithm employed, a sizable fraction of effort expended in nonlinear homogenization computations can and often is devoted to global line searching. (The fraction is largest with the memoriless BFGS algorithm and smallest with the Newton schemes.) During global line searching, nearly all operations are devoted to repeatedly forming the global residual vector **r**, the assembly of which is intensive in element level operations. Thus to achieve good performance, while reducing the expense of homogenization computations, element level operations must be optimized to take full advantage of the hardware available in the

computing environment. Accordingly vectorization and parallelization of element operations for three-dimensional trilinear continuum elements with general nonlinear material behaviors is considered here.

On vector–parallel machines, vectorization [55] allows for efficient usage of a given CPU and can thus substantially reduce computing costs. Parallelization [56] follows vectorization and its primary advantage is that it reduces throughput time. The FORTRAN code employed in this study has been optimized on Cray machines; the same basic principles apply as well to other vector–parallel machines and even to many workstation hardwares which now emulate vector–parallel machines.

Operations at the element level are divided between formation of the element matrices (shape functions N, strain displacement matrices $\mathbf{B}$, element stiffness matrices $\mathbf{k}_e$, and element force vectors $\mathbf{r}_e$) and solving nonlinear constitutive equations at each integration point. To provide a framework for this discussion, the operations required to form the global internal force vector for a group of eight-noded trilinear hexahedral continuum elements is provided in Box 3 through a sequence of generic subroutine calls.

```
do (l = 1, numel, 8! process eight elements at a time
   call htl-lcoord   ! localize coordinates X
   call htl-cshgg    ! compute shape functions N
   call htl-cb       ! form strain-displ. matrices B
   call htl-disp     ! localize displacement d
   call htl-strain   ! computes strains ε = Bd
   call eoslib       ! update stresses σ = σ(ε)
   call htl-btsig    ! element force r_e = ∫_Ωe B^T σ dΩ_e
   call addrhs       ! assemble global force vector
enddo
```

Box 3. Operations for eight-node hexahedral continuum element.

To achieve the highest possible computational speed (floating point operations per CPU-second) in element operations it is desirable to have both the formation of element matrices and the solution of constitutive equations vectorized. In the htl-prefixed routines of Box 3, the code processes eight elements at a time, and thus 64 stress points at a time, assuming that eight-point quadrature is used to integrate each element. (Note that on vector Crays each CPU is equipped with 64 vector registers, hence the appearance of this number. The restarting of vector pipelines is minimized by breaking loops up into integer multiples of 64 iterations, where loop "iterations" means the number of passes through a loop.) While the vectorization of most element operations is quite straightforward, vectorization of the constitutive models to process 64 stress points simultaneously is much less so.

The authors' experience to date in vectorizing constitutive model routines has been limited to single surface plasticity and viscoplasticity models which use operator-splitting predictor–corrector integration algorithms. For the fiber composite homogenization computations in Section 4 a vectorized $J-2$ plasticity model is employed; computing experience with a vectorized anisotropic quadratic viscoplasticity model was reported elsewhere [20, 21]. A vectorizable integration algorithm (processing NSTRESS stress points at a time) for a general single-surface plasticity model is provided below in Box 4. The first and third loops of Box 4, in which all of the actual work is done, are vectorizable.

```
input parameters: NSTRESS, FTOL
l = 0, ncon = 0
while (l < NSTRESS)      ! check yield criterion
  l = l + 1
  form elastic predictors σ_l^tr, q_l^tr
  if (f_l(σ_l^tr, q_l^tr) ≤ FTOL) then ! point is elastic
    icon_l = 1, idm_l = 0, ncon = ncon + 1
  else
    icon_l = 0, idm_l = 1
  endif
endwhile
if(ncon = NSTRESS) return ! all points elastic
while (ncon < NSTRESS)
  while(l < NSTRESS)
    l = l + 1
    if (idm_l = 1 and icon_l = 0) then
      perform return map iteration→f_l
      if (|f_l| < FTOL)
        icon_l = 1, ncon = ncon + 1
        perform final update of σ_l, q_l
      endif
    endif
  endwhile
endwhile
return
```

Box 4. Vectorized stress update for single-surface plasticity.

Optimal performance is achieved in the algorithm if load-balancing is achieved over the vectorized loop iterations. Practically, this occurs if the stress state at each quadrature point is either elastic or plastic. When all points are plastic, even better performance can be realized if roughly the same number of iterations are required to achieve convergence in the return-mapping for all points. Thus stress points which converge early do not have to wait long for the remainder to converge.

While single surface plasticity models are rather easy to vectorize, since a particular stress point has only one of two possibilities: elastic, or plastic, where plastic involves only a single active surface, vectorized implementations of intersecting multiple surface plasticity models as presented by Simo *et al.* [57] would be much more difficult to achieve since each stress point would have a larger number of possibilities: elastic, or plastic, where plastic could involve an indeterminate combination of active surfaces at a given time. The masonry homogenization computations of Section 4 involve a two-surface

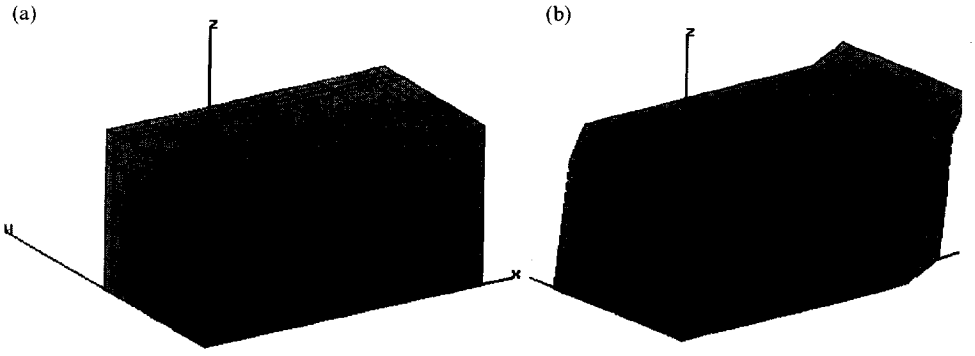

Fig. 3. (a) Undeformed unit cell; and (b) deformed unit cell of masonry following stress-controlled S_{13} shear test (deformation magnification = 46.5).

plasticity model of this type which is difficult to vectorize.

4. SAMPLE COMPUTATIONS

In the following subsections, sample analysis computations on inelastic composites are performed to present a rough gauge on the absolute costs associated with the analysis method, and to assess the relative performance of the solution algorithms discussed. The homogenization techniques presented are general enough to accommodate broad classes of constitutive models including both hardening and softening behaviors. For brittle, softening behaviors, however, special precautions must be taken to avoid mesh-dependency in results and to compensate for loss of positive definiteness in the global tangent operators. Since these precautions are beyond the scope of the current effort, attention is restricted in the following computations to usage of elastic–perfectly plastic constitutive models.

4.1. *Elasto-plastic masonry*

As part of an effort to assess the seismic worthiness of the Hagia Sophia in Istanbul, Turkey (AD 535), the limit strength properties of the structure's masonries were studied using computational homogenization. Macrostructure of the masonries were observed from the structure, while the individual brick and mortar mechanical properties were estimated from the data of Penelis [58] who studied a contemporaneous structure.

The macrostructure of the unit cell employed for consideration here is characteristic of a thickly jointed brick masonry found in upper portions of the Hagia Sophia, having brick dimensions l_1, l_2 and l_3, with aspect ratios $l_1/l_2 = 2$ and $l_1/l_3 = 2$. The relative thickness of all mortar joints t is given by the ratio $t/l_3 = 0.25$. In this study, the unit cell consists of a single brick and its three encompassing mortar joints in the X_1, X_2 and X_3 directions. With the particular meshing scheme employed, each mortar joint in the cell had three elements through its thickness, in a mesh containing 936 nodes and 672 continuum elements (Fig. 3). Eight-node trilinear hexahedral continuum elements were used with eight-point gaussian quadrature and a mean-dilational B-bar formulation [59]. Shear, compressive and tensile stress-controlled loading tests were performed on the cell measure its limit states in stress space.

The inelastic constitutive behavior of both the brick and mortar phases was represented with a two-surface elasto-plasticity model having a Drucker–Prager failure envelope and a circular tension cap (Fig. 4). The model was implemented using a fully implicit backward Euler integration algorithm along with consistent tangent operators. Material and geometric parameters of the brick and mortar, are summarized in Table 1.

The masonry computations were performed on a 2-CPU (R8000) SGI workstation with 192 Mb of shared RAM. The global solution algorithm was the modified Newton algorithm (Box 1) in conjunction with a skyline equation solver [11]. Sloan's nodal reordering algorithm [60] was also used to mitigate the storage requirements with these computations. Compatible surface elements [38] were employed to enforce periodicity. Naturally, as the limit state was approached in each test, the macroscopic stress increments were reduced. Results are summarized in Table 2 and sample stress–strain plots for the effective medium are shown in Fig. 5.

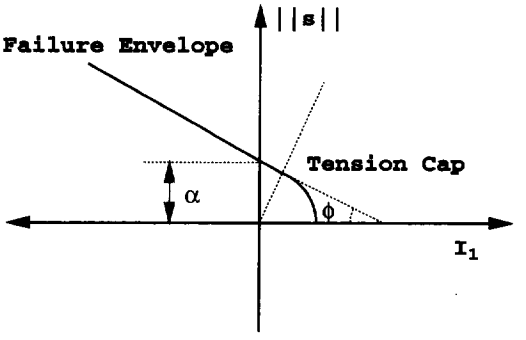

Fig. 4. Two-surface plasticity model used for bricks and mortar in homogenization computations.

Table 1. Constitutive model parameters of brick and mortar phases

Parameter	Brick	Mortar
λ(GPa)	2.61	1.64
μ(GPa)	1.12	1.09
α(MPa)	7.165	2.867
ϕ(degrees)	5.711	7.711

4.2. *Aligned fibrous composite*

The unit cell of a short, aligned graphite fiber–elastomeric epoxy matrix composite is now considered. The individual fibers have a diameter of 8 μm and a length of 90 μm. End-to-end spacing between fibers was 10 μm, while the closest lateral spacing between fiber axes was 10 μm. Both phases were modeled as elastic–perfectly plastic with a von Mises yield criterion; material property values for both phases are shown in Table 3. The plasticity model, which vectorized in accordance with Box 4, was implemented using a fully implicit backward Euler integration algorithm and consistent tangent operators.

The fiber composite unit cell for this computation (Fig. 6) comprised 5376 hexahedral continuum elements, 6061 nodes and 16,126 unrestrained nodal degrees of freedom, and was tested in a uniaxial strain mode along the fiber's long (X_3) axis. The strain-controlled test was performed in 40 load steps (20 loading and 20 unloading). Figure 7 shows the macroscopic stress–strain loading/unloading response of the composite. Using the three solution algorithms presented in Section 4, the same computation was performed on both a Cray C90 supercomputer, and on a 2-CPU R8000 SGI workstation. A summary of the costs of this computation, and of the relative performance of the alternative solution algorithms is presented in Table 4 which shows that if sufficient real memory is available, Newton's method with direct equation solvers is much faster than the iterative solution algorithms. While the iterative methods require much less memory, they take considerably more CPU time.

5. TOPOLOGY DESIGN OF MACROSTRUCTURE

5.1. *Distribution of materials*

In preceding sections, computational homogenization was applied to obtain response properties of composites having fixed design configurations. In macrostructural topology optimization, the design of the composite (the distribution and arrangement of materials present) is systematically varied to improve targeted response properties. A general method is presented that can be used both to find optimal material combinations (based on mechanical considerations) and to find their topological arrangement.

Once a FEM discretization of the starting unit cell has been constructed and set of N candidate materials selected that can feasibly go into the composite, a system is required to describe the material combinations and their spatial, geometric distribution. In the proposed method, a vector of continuous, real design variables $\mathbf{b} \in \mathscr{R}^{NEL \cdot N-1}$ contains this information. (Advantages of the continuous, real design variable approach over the alternative discrete integer design variable method have been pointed out by Strang and Kohn [61].) If, for example, the FEM mesh of the unit cell contains NEL elements, the design vector $\mathbf{b}$ has the definition

$$\mathbf{b} \equiv \{b_1, b_2, \ldots, b_{NEL}\} \tag{43}$$

where

$$b_i \equiv \{\phi_{i_1}, \phi_{i_2}, \ldots, \phi_{i_{N-1}}\} \quad \text{for } i \in \{1, 2, \ldots, NEL\}. \tag{44}$$

That is, the full vector of design variables $\mathbf{b}$ is comprised of NEL element level contributions, and each element level contribution b_i further consists of $N-1$ material volume fraction contributions $\{\phi_{i_1}, \phi_{i_2}, \ldots, \phi_{i_{N-1}}\}$ from the N candidate materials. This allows each of the N candidate materials to be arbitrarily distributed through the unit cell. To illustrate, if in a given element i, $\phi_{i_1} = 0$, then material 1 is not present in this element, whereas if $\phi_{i_N} = 1$, then the Nth material completely occupies the element. Natural constraints upon the elemental volume fractions are that

$$\sum_{j=1}^{j=N} \phi_{ij} = 1, \quad \text{for each } i \in \{1, 2, \ldots, NEL\} \tag{45}$$

and

$$\phi_{ij} \in [0, 1] \quad \text{for } j \in \{1, 2, \ldots, N\}. \tag{46}$$

Table 2. Summary of stress-controlled limit analysis homogenization of masonry

Limit analysis test	Limit (MPa)	Memory (Mw)[1]	CPU (min)
Compressive S_{11}	−7.39	2.71	31.74
Tensile S_{11}	+2.52	2.71	22.69
Compressive S_{33}	−7.35	2.71	33.05
Tensile S_{33}	+2.51	2.71	29.27
Shear S_{13}	2.08	2.71	34.86

[1]A Mw denotes 10^6 words, where the word length is eight bytes.

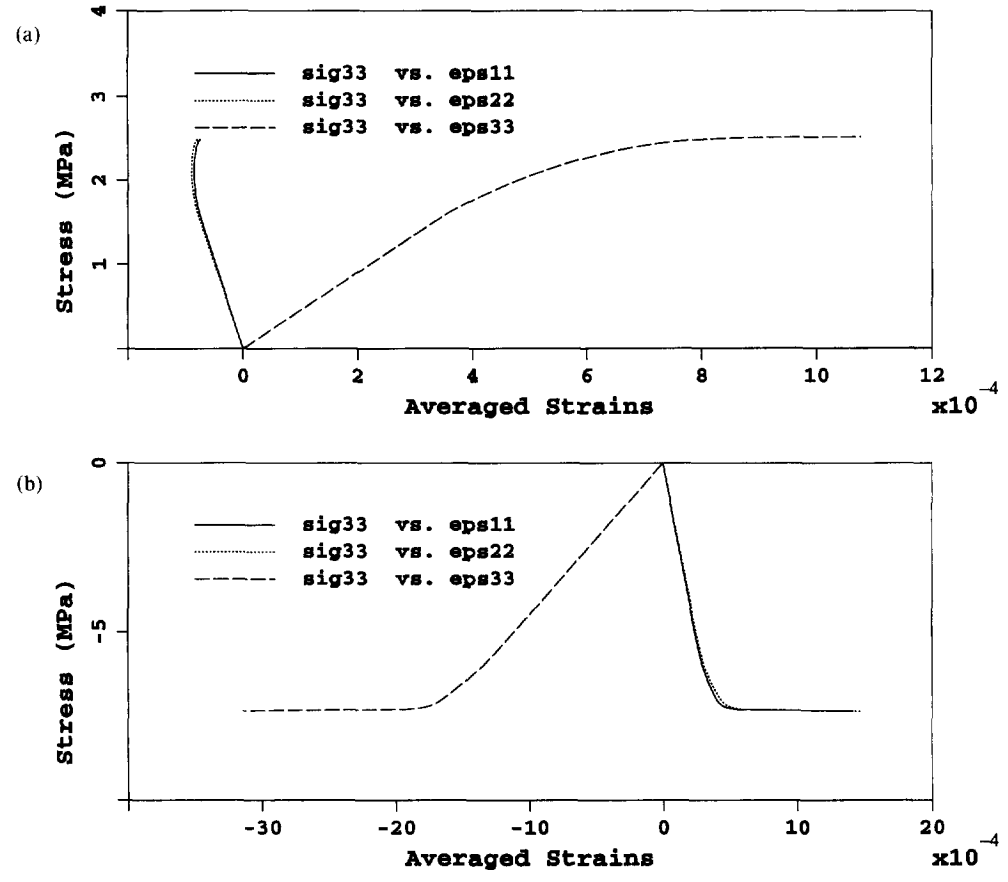

Fig. 5. Macroscopic stress–strain relations from: (a) stress-controlled tensile strength test; and (b) stress-controlled compressive strength test on masonry.

Material cost constraints can optionally be imposed upon the designed composite by specifying upper limits on the global volume fraction of each candidate phase:

$$\langle \phi_j \rangle - C_j \leqslant 0, \quad \text{for } j \in \{1, 2, \ldots, N\}, \tag{47}$$

where C_j is the maximum permissible value of the global volume fraction for the jth material phase in the composite's unit cell.

5.2. *Constitutive mixing rules*

Since each finite element of the unit cell model contains N material volume fractions, a critical issue is how these materials are combined to form element level stress–strain relations. In single-phase structural topology applications, the frequently addressed issue is where to put the solid material and where to omit it. For these applications mixing rules combining a single solid phase and a void phase have proven highly effective with the hardkill–softkill rule [2, 8] and the structured porous solid mixing rule [19] being quite popular. For topological design of composite materials the problem is somewhat more complicated in that mixing rules for N general elastic or inelastic solid constituent phases are required. The two classical mixing rules employed here (Fig. 8) satisfy these requirements in that they can be applied to both elastic and inelastic materials and yet are very simple in that they assume no "microstructure" in the mixture. (The objective of this work is to solve for macrostructure at the unit cell length scale, not at the element length scale.) The Voigt mixing rule assumes that all constituent phases present at a point in space share the same total strain ϵ; accordingly, the total stress at the point of interest is the weighted sum of the partial stresses:

$$\sigma(\mathbf{X}) = \sum_{j=1}^{j=N} \phi_j \sigma_j[\epsilon(\mathbf{X})]. \tag{48}$$

The alternative Reuss mixing rule assumes that all constituent phases present at a point in space share kthe same stress σ; by this mixing rule, the total strain

Table 3. Constitutive model parameters of fiber and matrix phases

Parameter	Fiber	Matrix
E(GPa)	260.0	0.690
ν	0.35	0.350
Y_0(MPa)	35,000	30.00

Y_0 denotes von Mises yield stress taken to match nominal compressive strengths of the phases.

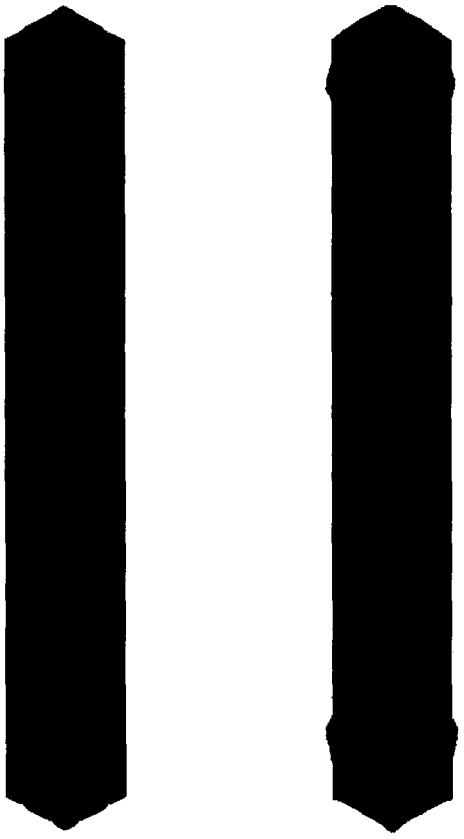

Fig. 6. (a) Undeformed unit cell; and (b) deformed unit cell of graphite fiber composite following strain-controlled axial $\mathbf{E}_{33}$ test (deformation magnification = 9.5).

ϵ at such a point is the weighted sum of the individual strains:

$$\epsilon(\mathbf{X}) = \sum_{j=1}^{j=N} \phi_j \epsilon_j[\sigma(\mathbf{X})]. \tag{49}$$

For inelastic constitutive material behaviors, the constant Reuss mixing rule is somewhat more cumbersome to implement numerically than the constant strain rule. Details on a robust implementation of the Reuss mixing rule are provided in Ref. [62].

Using simple energy arguments [37], it can be shown that the Voigt and Reuss mixing rules provide, respectively, upper and lower bounds on both the strength and stiffness characteristics of the mixture. Realizing that this is the case, the choice of which mixing rule to use depends on the quantity being optimized. When designing composite macrostructure to optimize effective stiffness and strength, the compliant constant stress mixing rule works best; in design of composite macrostructure to optimize specific compliances, the stiff constant strain rule gives better performance. For the overall optimization method to give sound and meaningful physical solutions, the resulting terminal macrostructure must asymptotically aggregate into regions of distinct material phases (that is, for example, asymptotic black and white solutions should be obtained for the two-material problem). In the limit where true "black and white" terminal macrostructures are achieved, the computed effective properties of the composite in the terminal state are independent of the mixing rule.

5.3. *Design sensitivity*

Having defined a numerical model of the composite unit cell that includes mechanisms for describing and varying material combinations, their spatial distributions and constitutive mixing rules, the remaining task is to specify objective functionals and to perform the optimization computations. All response functionals Ψ defined for the unit cell, whatever combinations of $\{\sigma, \epsilon, \mathbf{S}, \mathbf{E}\}$ they include, can ultimately be expressed in terms of the displacement field $\mathbf{u}(\mathbf{X}, \mathbf{b})$ on $\bar{\Omega}_s$ and the design vector $\mathbf{b}$, that is $\Psi = \Psi[\mathbf{u}(\mathbf{b}), \mathbf{b}]$. Specific functionals that target global stiffness and/or strength properties of the composite are defined and the macrostructure in the unit cell is then systematically varied by changing $\mathbf{b}$ to minimize them.

In any gradient based [1st order] optimization algorithm [53], it is essential that the total design gradient of the objective functionals be accurately and efficiently computable. That is, we must be able to compute

$$\frac{\mathrm{d}\Psi(\mathbf{b}, \mathbf{u})}{\mathrm{d}\mathbf{b}} = \frac{\partial \Psi}{\partial \mathbf{b}} + \frac{\partial \Psi}{\partial \mathbf{u}} \frac{\partial \mathbf{u}}{\partial \mathbf{b}}. \tag{50}$$

While the first term in this variation is easy to compute, the second term requires somewhat more effort. For clarity and simplicity, the method is here demonstrated on linear elastic composites. Treatment of more general nonlinear inelastic behaviors is treated in Ref. [63]. Given the restrictions imposed here, the adjoint sensitivity method of Arora and Cardosa [64] can be efficiently employed.

The adjoint sensitivity principle calls for introduction of an augmented Lagrangian as follows:

$$L(\mathbf{u}^a, \mathbf{b}, \mathbf{u}) = \Psi(\mathbf{b}, \mathbf{u}) + W^a(\mathbf{u}^a, \mathbf{b}, \mathbf{u}), \tag{51}$$

in which

$$W^a(\mathbf{u}^a, \mathbf{b}, \mathbf{u}) = \sum_{A \in \{n - n_g\}} (\mathbf{u}_A^a)^T \mathbf{r}_A. \tag{52}$$

In these expressions, $\mathbf{u}_A^a$ represents a field of kinematically admissible nodal variational displacements, hereafter called the adjoint displacement field,

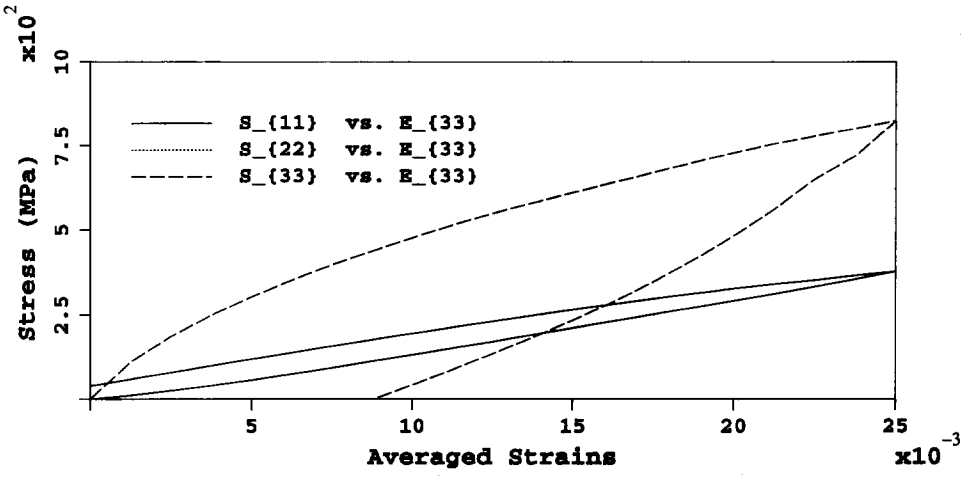

Fig. 7. Macroscopic stress–strain relations from $\mathbf{E}_{33}$ axial strain test on fiber composite.

and $\mathbf{r}_A$ is the nodal residual force vector for the discretized cell problem, eqn (23). Global equilibrium in the cell problem requires that $\mathbf{r}_A = \mathbf{0}\ \forall A \in \{n - n_g\}$. Hence for all admissible adjoint displacement fields $\mathbf{u}^a$, $W(\mathbf{u}^a, \mathbf{b}, \mathbf{u}) = 0$. Accordingly, it can be easily shown that the total design variation ($\bar{\delta}$) of W^a vanishes.

The fundamental concept in adjoint sensitivity analysis is to select the adjoint displacement field $\mathbf{u}^a$ such that the displacement variation ($\tilde{\delta}$) of the augmented Lagrangian vanishes for all possible design configurations. That is,

$$\tilde{\delta}L := \left(\frac{\partial \Psi}{\partial \mathbf{u}} + \frac{\partial W^a}{\partial \mathbf{u}}\right)\delta\mathbf{u} = 0. \tag{53}$$

In general, $\tilde{\delta}L$ vanishes for all $\delta\mathbf{u}$ if $\partial W^a/\partial \mathbf{u} = -\partial \Psi/\partial \mathbf{u}$. Substitutions of W^a from eqn (52) into this expression yields a linear system of algebraic equations that can easily be solved for the adjoint displacement field $\mathbf{u}^a$:

$$\frac{\partial \mathbf{r}}{\partial \mathbf{u}}\mathbf{u}^a = -\frac{\partial \Psi}{\partial \mathbf{u}}. \tag{54}$$

Now taking the total design variation of the augmented Lagrangian, eqn (51), one finds

$$\bar{\delta}L = \bar{\delta}\Psi + \bar{\delta}W^a$$

$$= \left(\frac{\partial \Psi}{\partial \mathbf{b}} + \frac{\partial \Psi}{\partial \mathbf{u}}\frac{\partial \mathbf{u}}{\partial \mathbf{b}}\right)\delta\mathbf{b} + \mathbf{r}^T\bar{\delta}\mathbf{u}^a \tag{55a}$$

$$+ (\mathbf{u}^a)^T\left[\frac{\partial \mathbf{r}}{\partial \mathbf{u}}\frac{\mathrm{d}\mathbf{u}}{\mathrm{d}\mathbf{b}} + \frac{\partial \mathbf{r}}{\partial \mathbf{b}}\right]\delta\mathbf{b}. \tag{55b}$$

The next to last term in eqn (55b) vanishes by the state equation, since $\mathbf{r} = 0$. Regrouping eqn (56) thus gives

$$\bar{\delta}L = \left(\frac{\partial \Psi}{\partial \mathbf{b}} + \frac{\partial W^a}{\partial \mathbf{b}}\right)\delta\mathbf{b} + \left(\frac{\partial \Psi}{\partial \mathbf{u}} + (\mathbf{u}^a)^T\frac{\partial \mathbf{r}}{\partial \mathbf{u}}\right)\frac{\mathrm{d}\mathbf{u}}{\mathrm{d}\mathbf{b}}\delta\mathbf{b}, \tag{56}$$

Table 4. Summary of strain-controlled computations on graphite–epoxy

Solution method	Required memory	CPU-hours (SGI-R8000)	CPU-hours (Cray C90)
Modified Newton with vectorized skyline solver. Factorizing tangent every eight iterations.	21.15 Mw	Insufficient memory	2.86
Modified Newton with JCG solver. Reforming the tangent every eight iteration.	3.10 Mw	20.8	12.5[1]
Memoriless BFGS	1.49 Mw	26.4	15.8[1]

[1]Estimated based on relative peek speeds of the machines (SGI is 300 MFLOPS per CPU, while C90 is 500 MFLOPS per CPU).

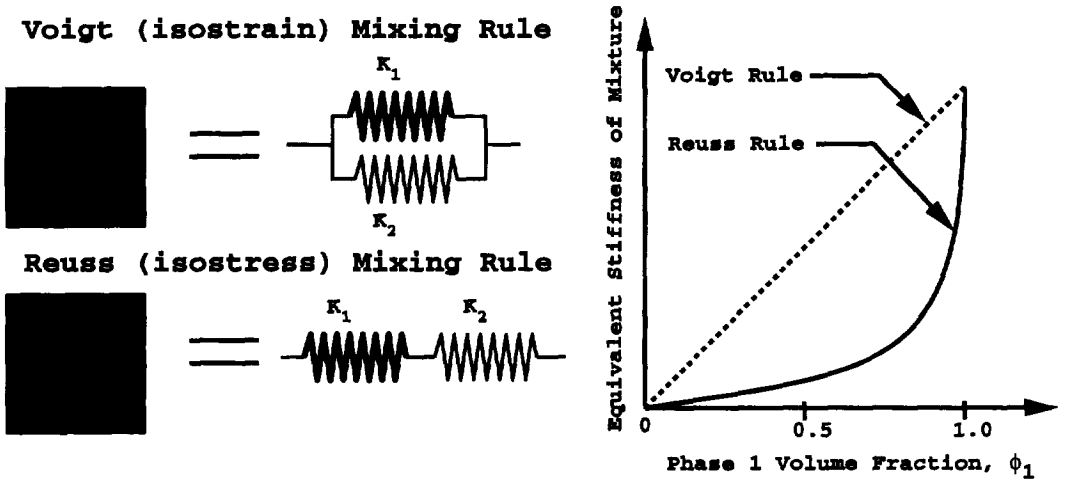

Fig. 8. Schematic illustration of the mixing rules used at the element level in topology optimization. The constant strain Voigt mixing rule provides an upper bound on stiffness, while the constant stress Reuss mixing rule provides a lower bound on stiffness.

in which the second term on the right vanishes by virtue of the specification of the adjoint displacement field according to eqn (54). Given further that $\bar{\delta} W^a = 0$, the desired displacement variation $\bar{\delta}\Psi$ can finally be written in the convenient form

$$\bar{\delta}\Psi = \bar{\delta} L = \left[\frac{\partial \Psi}{\partial \mathbf{b}} + \frac{\partial W^a}{\partial \mathbf{b}}\right]\delta \mathbf{b}. \tag{57}$$

Since it involves only partial derivatives, this expression for the design variations of the objective function can be easily computed.

Remark. In the linear solving phase of the adjoint sensitivity analysis, eqn (54), any of the direct or iterative methods discussed in Section 3 can be used to solve for $\mathbf{u}^a$. The expression $\partial \mathbf{r}/\partial \mathbf{u}$ in eqn (54) represents the global tangent stiffness matrix. If a direct solving algorithm is used for the FEM analysis, then this matrix already exists in factored **LU** form. In this case, solution of eqn (54) involves only a back-substitution operation. For optimum efficiency in sensitivity analysis, element level assembly of the vectors $\partial \Psi/\partial \mathbf{u}$, $\partial \Psi/\partial \mathbf{b}$ and $\partial W^a/\partial \mathbf{b}$ can be vectorized and parallelized.

5.4. *Illustrative examples*

The analysis software used in this effort is FENDAC [65] in which the homogenization and design sensitivity operations have been implemented, while the design optimization software is IDESIGN [66]. For the design problems that follow, an implicit sequential quadratic programming (ISQP) method using a limited memory BFGS constrained optimization algorithm in tandem with line searching was employed.

As presently constructed, many pultruded fiber composites consist of aligned E-glass fibers embedded in a resin epoxy thermosetting matrix. While such composites feature excellent axial stiffness and strength, their nonaxial properties suffer greatly in comparison. For example, the aligned fiber composites feature very modest transverse extensional strengths and stiffness, and even lower transverse shear stiffness and strengths. The problem of increasing the transverse extensional and shear stiffnesses of such composites while in no way compromising their good aligned axial properties is addressed in the following examples.

5.4.1. *Transverse normal stiffness*. Using realistic stiffness properties for both the fiber (E-glass) and the matrix (resin epoxy), the design method was applied to improve the transverse normal stiffness of the composite. For a realistic fiber volume fraction of 0.5, the transverse Young's modulus of the composite as currently designed is 9.1 GPa [regular square-packing of fibers assumed]. When the macrostructure of the composite is redesigned to optimize the transverse stiffness, the macrostructure shown in Fig. 9a is achieved and yields a predicted transverse Young's modulus of 34.6 GPa, which is nearly a three-fold improvement. This example indicates that alternative reinforcing configurations should be considered (other than aligned circular fibers) to improve non-axial stiffnesses.

5.4.2. *Transverse shear stiffness*. Using the same realistic elastic stiffness properties for both the fiber (E-glass) and the matrix (resin epoxy), the design method was subsequently applied to improve the transverse shear stiffness of the composite. For a realistic fiber volume fraction of 0.5, the transverse shear modulus of the composite as currently designed is 2.5 GPa (same assumption of regular, square packing invoked). When the macrostructure of the composite is redesigned to optimize the transverse

shear stiffness, the cellular macrostructure shown in Fig. 9b is achieved and gives a predicted transverse shear modulus of 9.1 GPa, which is roughly a 280% improvement.

From these two simple examples, it should be apparent that the proposed method is a very potent tool in macrostructural design of composites to achieve specific mechanical performance properties at no additional material costs. If additional materials had been considered in these examples (such as higher performance fiber and matrix phases), then even higher performance gains would have been demonstrated.

An important question that remains to be answered is how the effective material properties predicted by the optimized material structures and the FEM meshes used in the optimization process (Fig. 9) compare with the properties that would be predicted by more refined FEM meshes such as those that would be used in production computations. To answer this question, the topology shown in Fig. 9b was "post-processed" and remeshed (Fig. 10a) and then subjected to a pure macroscopic shear state (Fig. 10b). The effective shear modulus predicted by this computation is $C_{1212} = 10.6$ GPa as compared to the shear modulus $G_{1212} = 9.1$ GPa predicted by the "mixture" mesh. Clearly, the post-processing interpretation of the optimized topology is not exact, and some variations of the predicted mechanical properties are to be expected. A likely cause for at least part of this discrepancy is that while the mesh in Fig. 9b has a precise volume fraction for the glass phase of 50%, the mesh shown in Fig. 10a has a glass volume fraction of 51.5%. This slight increase in the glass fraction increases the shear modulus predicted by the post-processed production model.

5.5. *Parametric material design optimization*

In the previous subsection, a framework was established for nonparametric design optimization to obtain macrostructural topologies that significantly improve the mechanical performance of the composite. Having achieved significantly improved performance of the composite in the nonparametric topology optimization phase, the topology can then be refined in a secondary parametric shape optimization phase using techniques similar to those used in tailoring. For example, the optimized macrostructures shown in Fig. 9 can be parameterized as shown in Fig. 11 and then iteratively optimized. With each revision of the design parameters, the unit cell can be automatically remeshed and its properties predicted by computational homogenization. The authors have yet to implement this second stage in the design optimization process for composite macrostructures.

6. CLOSURE

Accurate and efficient methods have been proposed within the framework of the displacement finite element method for solving the unit cell homogenization problem for periodic composites. Using the homogenization framework, a general new procedure for designing the macrostructure of composites has been proposed and demonstrated.

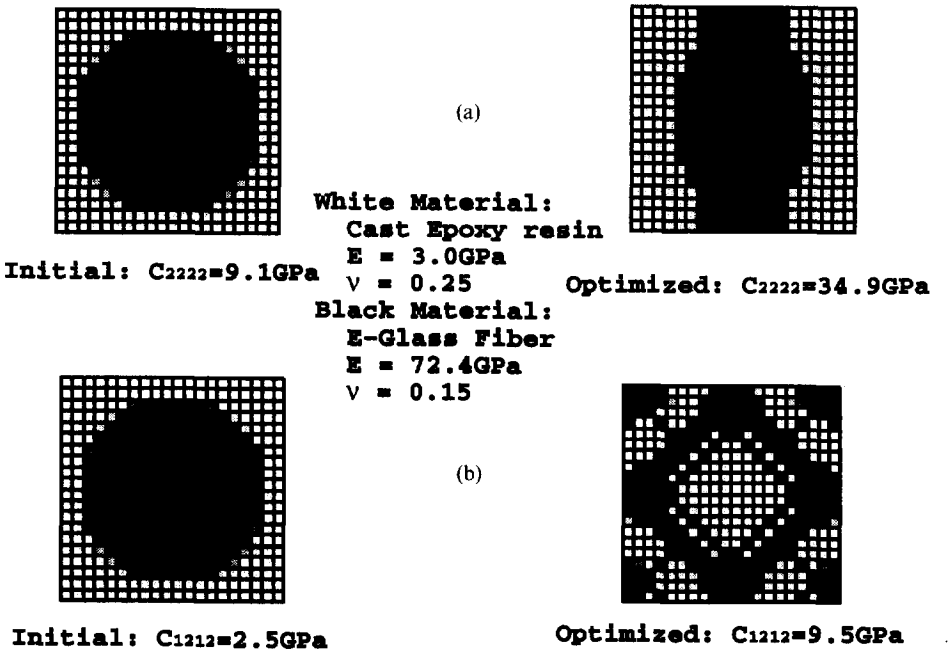

Fig. 9. Unit cells of initial and optimized macro-structures of an aligned fibrous pultruded composite: (a) a macrostructure designed to optimize C_{2222} with $\Psi = E_{22}$ under applied S_{22} loading; (b) a macrostructure designed to optimize C_{1212} with $\Psi = E_{12}$ under applied S_{12} loading.

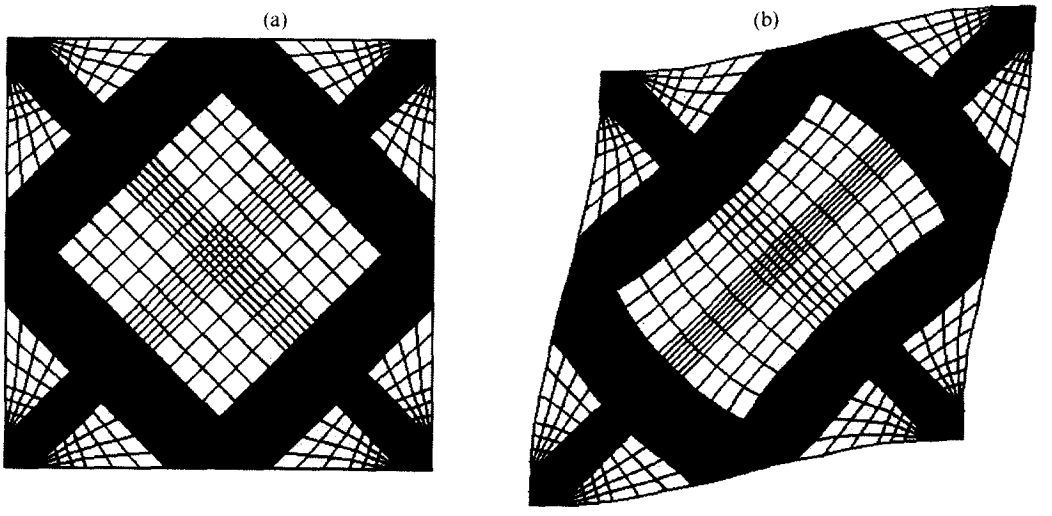

Fig. 10. Undeformed and deformed unit cells of remeshed and optimized cellular macrostructure for a glass–epoxy composite in a state of pure elastic macroscopic shear. The black material is E-glass, and the white material is resin epoxy. The computation shown predicts a shear modulus for the composite of $C_{1212} = 10.63\text{GPa}$. (a) Undeformed unit cell; (b) deformed unit cell in pure macro shear.

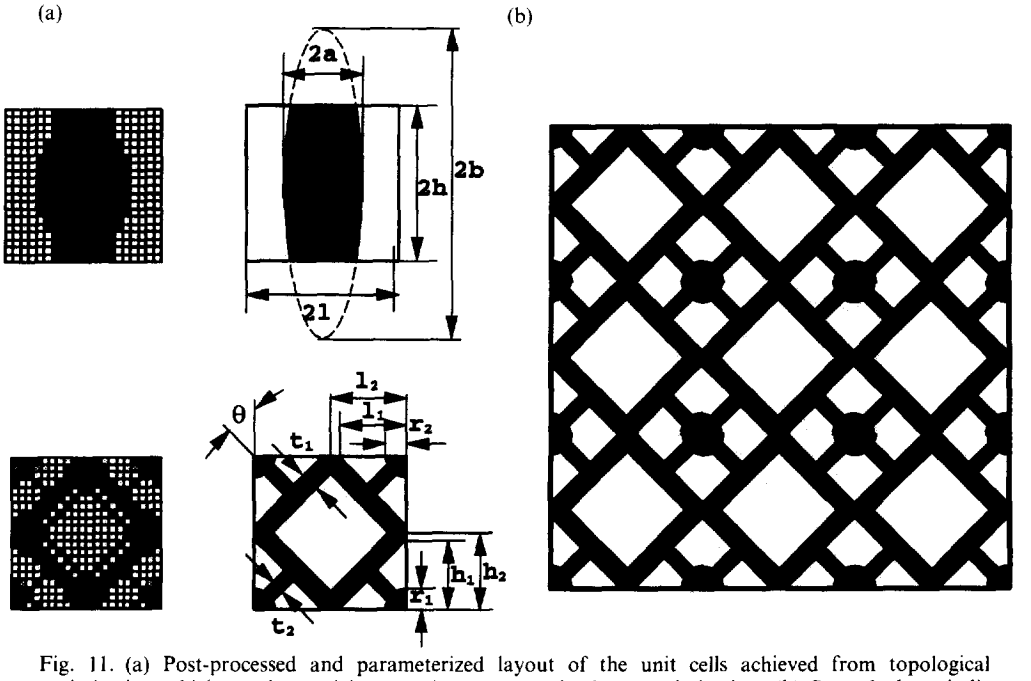

Fig. 11. (a) Post-processed and parameterized layout of the unit cells achieved from topological optimization which can be used in secondary parametric shape optimization. (b) Smoothed, periodic cellular macrostructure with 50–50 glass and epoxy volume fractions resulting from the shear stiffness optimal design.

The need for rapid and efficient methods of analyzing nonlinear structural and material systems has long been recognized; analysis and design of composites as proposed here gives added impetus to this drive.

Acknowledgements—The first author gratefully acknowledges fruitful discussions about optimization and design sensitivity aspects of this research with Professor Jasbir S. Arora. Computing resources for this effort were provided in part by the Pittsburgh Supercomputing Center.

REFERENCES

1. M. A. Da, N. Kikuchi, H.-C. Cheng and I. Hagiwara, Topology and shape optimization for structural dynamic problems. *ASME-PVP* **248**, 133–143 (1992).
2. E. Hinton and J. Sienz, Aspects of adaptive finite element analysis and structural optimization. In: *Advances in Structural Optimization*, pp. 1–25. Civil-Comp Press, Edinburgh (1994).
3. N. Kikuchi and K. Suzuki, Structural optimization of a linearly elastic structure using the homogenization method. In: *Composite Media and Homogenization Theory*, pp. 183–203. Springer, Berlin (1991).
4. H. P. Mlejnek and R. Schirrmacher, An engineer's

approach to optimal material distribution and shape finding. *Comput. Meth. appl. Mech. Engng* **106,** 1–26 (1993).
5. G. I. N. Rozvany, *Structural Design via Optimality Criteria: the Prager Approach to Structural Optimization*. Kluwer Academic, Dordrecht (1989).
6. E. Sandgren, E. Jensen and J. W. Welton, Topological design of structural components using genetic optimization methods. In: *Sensitivity Analysis and Optimization with Numerical Methods*, ASME-AMD 115, pp. 31–43. ASME, New York (1990).
7. K. Suzuki and N. Kikuchi, Shape and topology optimization by a homogenization method. *ASME-AMD* 115, pp. 15–30. ASME, New York (1990).
8. E. Ramm, K.-U. Bletzinger, R. Reitinger and K. Maute, The challenge of structural optimization. In: *Advances in Structural Optimization*, pp. 27–52. Civil-Comp Press, Edinburgh (1994).
9. B. H. V. Topping and M. Papadrakakis (Eds), *Advances in Structural Optimization*. Civil-Comp Press, Edinburgh (1994).
10. R. S. Lakes, Materials with structural hierarchy. *Nature* **361,** 511–515 (1993).
11. O. O. Storaasli, D. T. Nguyen and T. K. Agarwal, Parallel-vector solution of large-scale structural analysis problems on supercomputers. *AIAA J.* **28,** 1211–1216 (1990).
12. O. O. Storaasli, D. T. Nguyen and T. K. Agarwal, A parallel-vector algorithm for rapid structural analysis on high-performance computers. NASA Technical Memo 102614, Hampton, VA (1990).
13. R. Johanson, J. Fonseca, N. Kikuchi and P. Papalambros, Structural design for freeform fabrication using composite materials. In: *Proc. of the Solid Freeform Fabrication Symp.*, Austin, TX (1994).
14. R. Johanson, N. Kikuchi and P. Papalambros, Simultaneous topology and material microstructure design. In: *Advances in Structural Optimization*, pp. 143–150. Civil-Comp Press, Edinburgh (1994).
15. O. Sigmund, Design of material structures using topology optimization. Report S 69, Danish Center for Applied Mathematics and Mechanics, Technical University of Denmark, Lyngby (1994).
16. D. A. Saravanos and C. C. Chamis, Integrated mechanics for the passive damping of polymer matrix composites and composite structures. In: *M3D: Mechanics and Mechanisms of Material Damping*, ASTM Special Technical Publication, no. 1169, Philadelphia, PA, no. pp. 471–489 (1992).
17. C. Rabzak, D. Saravanos and C. C. Chamis, Optimal synthesis of hot composite laminates with interphase layers. NASA-TM-106326, NASA Lewis Research Center, Cleveland, OH (1993).
18. C. C. Chamis, P. L. N. Murthy and S. N. Singhal, Computational simulation of hot composite structures. NASA-TM-106200, NASA Lewis Research Center, Cleveland, OH (1993).
19. M. P. Bendsoe and N. Kikuchi, Generating optimal topologies in structural design using a homogenization method. *Comput. Meth. appl. Mech. Engng* **71,** 197–224 (1988).
20. C. C. Swan and A. S. Cakmak, A hardening orthotropic plasticity model for non-frictional composites: rate formulation and integration algorithm. *Int. J. numer. Meth. Engng* **28,** 839–860 (1994).
21. C. C. Swan and A. S. Cakmak, Nonlinear quasi-static and seismic analysis of the Hagia Sophia using an effective medium approach. *Soil Dyn. Earthq. Engng* **12,** 259–271 (1993).
22. A. Bensouan, J.-L. Lions and G. Papanicolaou, Asymptotic analysis for periodic structures. North-Holland, Amsterdam (1978).
23. J. C. Michel and P. M. Suquet, On the strength of composite materials: variational bounds and computational aspects. In: *Topology Design of Structures* (Edited by M. P. Bendsoe and C. A. Mota Soares), pp. 355–374. Kluwer Academic, Dordrecht (1993).
24. P. Ponte Castañeda, The effective mechanical properties of nonlinear isotropic composites. *J. Mech. Phys. Solids* **39,** 45–71 (1991).
25. J. R. Willis, On methods for bounding the overall properties of nonlinear composites. *J. Mech. Phys. Solids* **39,** 73–86 (1991).
26. L. V. Gibiansky and S. Torquato, Link between the conductivity and elastic moduli of composite material. *Phys. Rev. Lett.* **71,** 2927–2930 (1993).
27. C. A. Miller and S. Torquato, Improved bounds on elastic and transport properties of fiber-reinforced composites: effect of polydispersivity in fiber radius. *J. appl. Phys.* **69,** 1948–1955 (1991).
28. G. Milton, On characterizing the set of possible effective tensors of composites: the variational method and the translational method. *Commun. pure appl. Math.* **43,** 63–125 (1990).
29. G. W. Milton, Composite materials with Poisson's ratios close to -1. *J. Mech. Phys. Solids* **40,** 1105–1137 (1992).
30. V. Nesi and G. W. Milton, Polycrystalline configurations that maximize electrical resistivity. *J. Mech. Phys. Solids* **39,** 525–542 (1991).
31. J. W. Ju and T. M. Chen, Micromechanics and effective moduli of elastic composites with randomly dispersed inhomogeneities. In: *Macroscopic Behavior of Heterogeneous Materials from the Microstructure*, Vol. AMD 147, pp. 95–109. ASME, New York (1993).
32. P. V. McLaughlin and S. C. Batterman, Limit behavior of fibrous materials. *Int. J. Solids Struct.* **6,** 1357–1376 (1970).
33. P. V. McLaughlin, Plastic limit behavior and failure of filament reinforced materials. *Int. J. Solids Struct.* **8,** 1299–1318 (1972).
34. A. Dasgupta and R. K. Agarwal, Orthotropic thermal conductivity of plain-weave fabric composites using a homogenization technique. *J. Compos. Mater.* **26,** 2736–2758 (1992).
35. Y. Yi and S.-Y. Luo, Modeling of plain weave fabric composite under finite deformation, Vol. PVP 248 and NE 10, pp. 41–48. ASME, New York (1992).
36. T. Dutta, T. K. Ballabh and T. R. Middya, Green function calculation of effective elastic constants of textured polycrystalline materials. *J. Phys. D: appl. Phys.* **26,** 667–675 (1993).
37. J. Aboudi, *Mechanics of Composite Materials: a Unified Micromechanical Approach*, Chap. 9. Elsevier, New York (1991).
38. C. C. Swan, Techniques for stress and strain controlled homogenization of inelastic periodic composites. *Comput. Meth. appl. Mech. Engng* **117,** 249–267 (1994).
39. C. C. Swan and A. S. Cakmak, Homogenization and effective elastoplasticity models for periodic composites. *Commun. numer. Meth. Engng* **10,** 257–265 (1994).
40. P. Pegon and A. Anthoine, Numerical strategies for solving continuum damage mechanics problems involving softening: application to the homogenization of masonry. In: *Advances in Non-linear Finite Element Methods*, pp. 143–158. Civil-Comp Press, Edinburgh (1994).
41. J. M. Guedes, Effective properties for non-linear composite materials: computational aspects. In: *Topology Design of Structures* (Edited by M. P. Bendsoe and C. A. Mota Soares), pp. 375–394. Kluwer Academic, Dordrecht (1993).
42. P. M. Suquet, Approach by homogenization of some linear and nonlinear problems in solid mechanics. In: *Plastic Behavior of Anisotropic Solids, Proc. of the*

CNRS Int. Colloq. 319 (Edited by J. P. Boehler). CNRS, Paris (1985).
43. P. M. Suquet, Local and global aspects in the mathematical theory of plasticity. In: *Plasticity Today: Modelling Methods and Applications* (Edited by A. Sawczuk and G. Bianchini), pp. 279–310. Elsevier, Oxford (1985).
44. P. M. Suquet, Elements of homogenization for inelastic solid mechanics. In: *Homogenization Techniques for Composite Media* (Edited by E. Sanchez-Palencia and A. Zaoui), pp. 193–278. Springer, Berlin (1987).
45. C. Farhat, A Lagrange multiplier based divide and conquer finite element algorithm. *Comput. Syst. Engng* **31,** 149–156 (1991).
46. C. Farhat and F. X. Roux, A method of finite element tearing and interconnecting and its parallel solution algorithm. *Int. J. numer. Meth. Engng* **32,** 1205–1227 (1991).
47. E. L. Poole, N. F. Knight and D. D. Davis, High-performance equation solvers and their impact on finite element analysis. *Int. J. Numer. Meth. Engng* **33,** 855–868 (1992).
48. M. Geradin and M. Hogge, Solving systems of nonlinear equations. In: *The Finite Element Handbook* (Edited by H. Kardes-Tuncer). McGraw-Hill, New York (1987).
49. T. J. R. Hughes, R. M. Fenencz and J. O. Hallquist, Large-scale vectorized implicit calculations in solid mechanics on a Cray X-MP/48 utilizing EBE preconditioned conjugate gradients. *Comput. Meth. appl. Mech. Engng* **61,** 215–248 (1987).
50. M. J. D. Powell, Some convergence properties for the conjugate gradient method. *Math. Progm.* **11,** 42–49 (1976).
51. G. H. Golub and C. F. Van Loan, *Matrix Computations*. Johns Hopkins University Press, Baltimore, MD (1983).
52. D. F. Shanno, Conjugate gradient methods with inexact searches. *Math. Ops Res.* **3,** 244–256 (1978).
53. D. G. Luenberger, *Linear and Nonlinear Programming*. Addison-Wesley, Reading (1984).
54. H. Matthies and G. Strang, The solution of nonlinear finite element equations. *Int. J. numer. Meth. Engng* **14,** 1613–1626 (1979).
55. *CF77 Compiling System*, Vol. 3: Vectorization guide SG-3073.50. Cray Research, Mendota Heights, MN (1991).
56. *CF77 Compiling System*, Vol. 4: Parallel Processing Guide, SG-3074.50. Cray Research, Mendota Heights, MN (1991).
57. J. C. Simo, J. Kennedy and S. Govindjee, Non-smooth multisurface viscoplasticity. Loading/unloading conditions and numerical algorithms. *Int. J. numer. Meth. Engng* **26,** 2161–2185 (1988).
58. G. Penelis, Analysis of the Rotunda of Thessaloniki. In: *Hagia Sophia: from the Age of Justinian to the Present* (Edited by R. Mark and A. S. Cakmak). Cambridge University Press, Cambridge (1992).
59. T. J. R. Hughes, *The Finite Element Method: Linear Static and Dynamic Finite Element Analysis*. Prentice-Hall, Englewood Cliffs, NJ (1987).
60. S. W. Sloan, A Fortran program for profile and wavefront reduction. *Int. J. numer. Meth. Engng* **28,** 2651–2679 (1989).
61. G. Strang and R. V. Kohn, Optimal design in elasticity and plasticity. *Int. J. numer. Meth. Engng* **22,** 183–188 (1986).
62. C. C. Swan and I. Kosaka, Revss and Voigt Mixing Rules for variable topology material layout: part 2: structures with nonlinear materials (in press).
63. C. C. Swan and J. S. Arora, Topology design of material layout in structured composites of high stiffness and strength. *Struct. Optim.* (1996) (in press).
64. J. S. Arora and J. B. Cardosa, Variational principle for shape design sensitivity analysis. *AIAA J.* **30,** 538–547 (1992).
65. C. C. Swan, *FENDAC Users Manual and Methods Documentation*. University of Iowa, Iowa City, IA (1993).
66. J. S. Arora, T. Lin, O. Elwakeil and M. Wang, *IDESIGN Users' Manual Version 4.2*. University of Iowa, Iowa City, IA (1994).